Journal of Nuclear Materials 380 (2008) 46–58

Contents lists available at ScienceDirect

Journal of Nuclear Materials

journal homepage: www.elsevier.com/locate/jnucmat

Microstructural modelling of nuclear graphite using multi-phase models

C. Berre [a,*,1], S.L. Fok [b,2], B.J. Marsden [b], P.M. Mummery [c], T.J. Marrow [c], G.B. Neighbour [d]

[a] The Welding Institute (TWI Ltd.), Granta Park, Cambridge CB21 6AL, UK
[b] Nuclear Graphite Research Group, School of Mechanical, Aerospace and Civil Engineering, University of Manchester, Sackville Street, P.O. Box 88, Manchester M60 9QD, UK
[c] School of Materials, University of Manchester, Grosvenor Street, Manchester M1 7HS, UK
[d] Department of Engineering, University of Hull, Cottingham Road, Hull HU6 7RX, UK

ARTICLE INFO

Article history:
Received 28 April 2008
Accepted 15 July 2008

ABSTRACT

This paper presents a new modelling technique using three-dimensional multi-phase finite element models in which meshes representing the microstructure of thermally oxidised nuclear graphite were generated from X-ray micro-tomography images. The density of the material was related to the image greyscale using Beer–Lambert's law, and multiple phases could thus be defined. The local elastic and non-linear properties of each phase were defined as a function of density and changes in Young's modulus, tensile and compressive strength with thermal oxidation were calculated. Numerical predictions compared well with experimental data and with other numerical results obtained using two-phase models. These models were found to be more representative of the actual microstructure of the scanned material than two-phase models and, possibly because of pore closure occurring during compression, compressive tests were also predicted to be less sensitive to the microstructure geometry than tensile tests.

1. Introduction

Due to its very good thermo-mechanical and fast neutron moderation properties, Gilsocarbon nuclear grade graphite is used as a moderator and structural component of advanced gas-cooled reactors in the UK (AGR). Gilsocarbon is a near-isotropic polycrystalline graphite with a microstructure composed of spherical coke filler particles embedded in a coal–tar pitch matrix, which is graphitized, with around 20% of porosity generated via the different stages of the manufacturing process [1,2]. During operation in a carbon dioxide cooled reactor such as the AGR, nuclear graphite is subjected to fast neutron irradiation and radiolytic oxidation which, over time, significantly increases the internal porosity of the microstructure of the graphite components. For practical reasons, and under specially controlled conditions, thermal oxidation is often used in research programmes to simulate this weight loss due to radiolytic oxidation of graphite [3]. However, it should be noted that since the outlet temperature in AGRs is below $T = 650$ °C, thermal oxidation in CO_2 does not occur in these types of reactors.

The mechanical properties of nuclear graphite have been related to microstructural changes due to oxidation [3]. These changes can be investigated using a non-destructive imaging technique such as X-ray micro-tomography, from which three-dimensional images of the microstructure can be obtained. Other imaging techniques, such as focused ion beam dispersive spectroscopy (FIB-EDX), are also available to obtain very high-resolution images of the microstructure [4]. Lasagni et al. [4] used FIB-EDX to quantitatively characterise the microstructure of aluminium alloys containing micro-particles of silicium. Image resolutions were between 60 nm and 300 nm, however, because of the very large database generated during three-dimensional reconstruction, the volume of study was limited a few tens of a micron cube. Because of the relative average pore size of nuclear graphite, this volume would not be suitable to analyse pore changes due to thermal oxidation. Using X-ray micro-tomography on bulk samples (i.e. ~10 mm size), images can be obtained with typical resolutions of about 10 μm [5], although higher resolutions can be obtained from more powerful synchrotron facilities [6,7]. These high-resolutions thus allow the effects of microstructural changes on the mechanical properties to be described in three-dimensions using a quantitative [5] or an image-based finite element analysis [8]. While quantitative analyses employ empirical or analytical methods, image-based modelling makes use of finite element analysis to calculate the mechanical properties of a specimen directly from the tomographic scan of the microstructure. Finite element analysis using microstructural models has now extensively been used to study

* Corresponding author. Tel.: +44 1223 899 000; fax: +44 1223 890 689.
E-mail address: Christophe.Berre@twi.co.uk (C. Berre).
[1] Work performed while at the Nuclear Graphite Research Group, The University of Manchester, UK.
[2] Present address: University of Minnesota, School of Dentistry, Moos Health Sciences Tower, 515 Delaware Street SE, Minneapolis, MN 55455, USA.

0022-3115/$ - see front matter © 2008 Elsevier B.V. All rights reserved.
doi:10.1016/j.jnucmat.2008.07.006

the relationships between elastic properties and the microstructure, in particular porosity, of cellular materials [6] and concrete [9].

In this technique, a high-resolution image of the microstructure can be converted into highly accurate finite element three-dimensional meshes using commercially available software packages such as Scan^{IP} and Scan^{FE} [10]. Subsequent finite element analysis can then be performed using a commercial code such as ABAQUS [11] to investigate the stress field within the material microstructure and to calculate the effective mechanical properties of the specimen. This technique has been successfully applied to thermally oxidised isotropic graphite using two-phase numerical models [12,13].

The numerical accuracy of the solution given by image-based modelling techniques largely depends on the geometry and quality of the finite element mesh. The finite element mesh geometry depends on the resolution of the initial tomographic image, i.e. the smallest observable size of a detail, and also the pre-processing technique used to transform a tomographic image into a finite element mesh. The pre-processing method is very important for the resulting mesh and therefore numerical solution, as it involves segregating the different material phases of the initial image. It is important to take care pre-processing the tomographic image in order to produce a reasonably accurate finite element mesh in which the aspect ratio and distortion of the elements is kept to a minimum in order to achieve a well converged numerical solution. As tomographic images are composed of greyscale elements, the pre-processing step is often performed using a greyscale threshold. However, the application of a greyscale threshold to give a binary structure of pores and solid introduces some uncertainties to the geometric accuracy of the resulting finite element mesh.

In this paper, in order to obtain a more reliable mesh and hence numerical solution, a multi-phase finite element method has been used, in which, instead of the mesh having empty spaces with zero elastic modulus to represent the internal graphite porosity, these pores are modelled using finite elements with elastic modulus very close to zero. This helps to avoid singularities and ill-conditioning of the various mesh solution. In an improved modelling technique, the image greyscale was first calibrated to the density, ρ, of the scanned specimen using a step-wedge method (see Section 2 and [5]). Secondly, tomographic images were segmented into multiple phases of different densities according to their greyscale. Using the Simpleware package[3] [10], Young's modulus (E) of each phase was defined according to the density (ρ) using the power form $E = A\rho^B$, where A and B are constants. This relationship was implemented in the image segmentation software ScanIP™ thus allowing multiple phases to be defined in the finite element model. Hence, the resulting finite element model does not require the definition of a particular greyscale threshold. Using this image-based modelling technique, Young's modulus of thermally oxidised specimens was calculated by a linear elastic analysis whereas the compressive and tensile strengths were calculated using a strain-based failure model defined for each phase of the model. The numerical predictions were then compared to experimental data available in the literature.

2. X-ray micro-tomography

In X-ray micro-tomography, an X-ray beam can be generated from the collision between a flux of electrons and a filament of copper [5]. The acquisition device used for the acquisition of the X-ray micro-tomography dataset was an X-Tek HMX-225 laboratory instrument. The maximum energy and the intensity of the electron beam was set to 50 keV and 75 μA (microamperes), respectively. To remove the low energy rays from the emitted beam which might interfere with those of higher energies, an aluminium filter with a thickness of 0.25 mm was placed in front of the X-ray source. A series of two-dimensional radiographs of a scanned specimen was then obtained, which was then converted into a three-dimensional dataset using a reconstruction algorithm. The resulting tomographic images can be either coded in 8 bits or 16 bits, using a greyscale containing respectively 256 (2^8) or 65 536 (2^{16}) grey levels. The image greyscale is related to the density of the material, higher densities being represented by brighter voxels.[4] In tomography, the intensity (I) received by the receptor is related to the intensity I_0 emitted by the X-ray source by Beer–Lambert's law [14]:

$$I = I_0 \exp(-\mu t), \tag{1}$$

where μ is the attenuation factor, and t is the thickness of the scanned specimen.

The density of each specimen can then be calculated from the image greyscale if the attenuation factor μ is known. The calibration required to determine μ was realised using a step-wedge method [14].

2.1. Step-wedge method

The step-wedge method consists of measuring the transmitted intensity of the X-ray beam, using a reference material having a known uniform density and a similar chemical composition to the specimens to be scanned. This should be done at the same time as the experimental observations, to prevent error from aging of the filament. The density of the material is known and it is assumed to be uniform along the X-ray path. For graphite specimens, highly oriented pyrolitic graphite (HOPG) is suitable for the calibration since its bulk density ($\rho_{HOPG} = 2150\ kg/m^3$) is close to the theoretical value of pure graphite crystals, i.e. $\rho_c = 2260\ kg/m^3$. The transmitted intensity (I) of the X-ray beam was measured for different thicknesses of HOPG (Fig. 1). Using the chosen energy settings, the linear attenuation factor $\mu = 0.762\ cm^{-1}$ was obtained from the slope of Fig. 1 using Beer–Lambert's law Eq. (1).

2.2. Image acquisition

A set of 12 Gilsocarbon specimens was thermally oxidised up to 1350 h in a carbon dioxide environment at 700 °C. Initially, these specimens were 15-mm long cylinders with a 9-mm diameter. The thermal oxidation procedure was identical to the one described in [15] and thermal oxidation rates up to 40% weight loss were obtained. The thermally oxidised specimens were then scanned using X-ray micro-tomography as described above. X-ray micro-tomography datasets of virgin and thermally oxidised Gilsocarbon specimens were then obtained with a voxel resolution of 19 μm. This technique is non destructive and allows the microstructure of the specimen to be visualised in three-dimensions. In the three-dimensional images extracted from the original tomographic dataset and shown in Fig. 2, the effects of thermal oxidation can clearly be seen in Fig. 2(b).

The effect of thermal oxidation on the microstructure of graphite is shown in more detail in Fig. 3 on slices taken from X-ray micro-tomography datasets of virgin and thermally oxidised graphite. Fig. 3 shows that the microstructure of graphite is subjected to significant changes due to oxidation. In Fig. 3(b), a large part of the specimen became detached, possibly due to non-uniformity of thermal oxidation throughout the volume. The level of oxidation is then higher along the edges of the specimen than at the centre.

[3] Simpleware website: www.simpleware.co.uk/.

[4] A voxel is the three-dimensional analogue to a two-dimensional pixel.

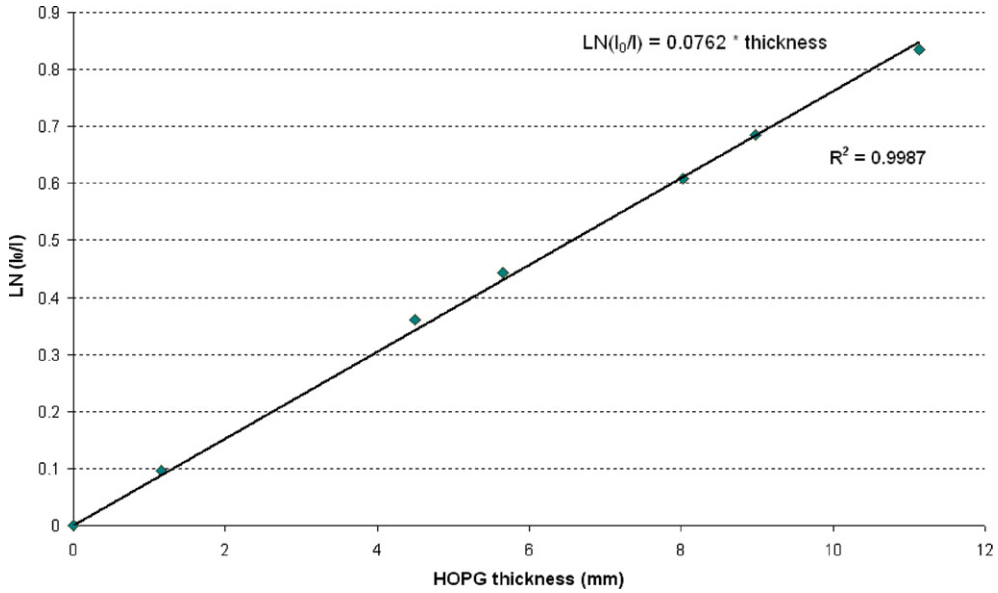

Fig. 1. Measurement of the attenuation factor from the logarithm of the ratio I/I_0 with increasing thickness of HOPG.

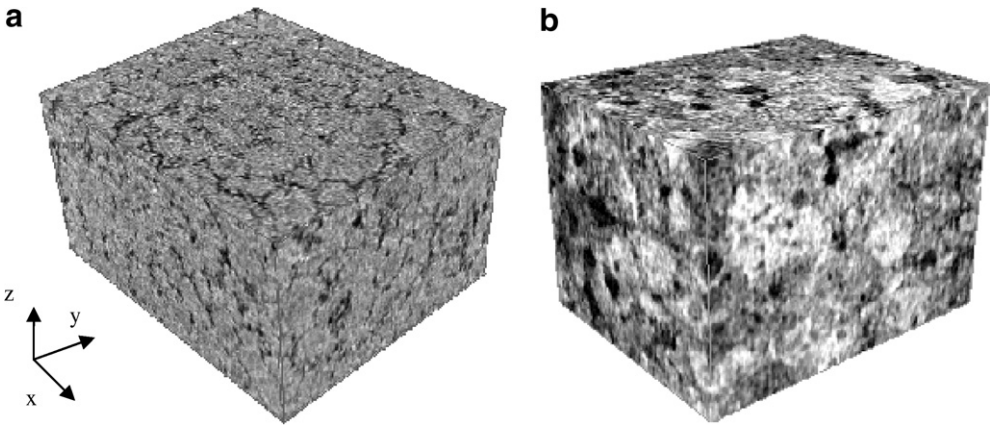

Fig. 2. Three-dimensional tomography images of (a) virgin and (b) thermally oxidised 40% weight loss graphite (resolution = 19 μm). Both images show a volume around 8 mm × 6.6 mm × 5.5 mm of the scanned specimens (Regions of higher attenuation are lighter coloured).

Locally, some areas such as filler particles are also relatively dense after oxidation, which is shown by the brighter elements in the image (Fig. 3(d)), when compared to the matrix. Fig. 3(d) also shows that large inter-granular pores appear more pronounced after oxidation, and filler particles become easily differentiable as a result of the preferential oxidation in the matrix.

2.3. Calculated density

The calculation of the density of nuclear graphite using X-ray micro-tomography images has already been investigated by Babout et al. [14]. Based on this approach, the local density of the material was related to the brightness of the voxel in the image. Three-dimensional images resulting from X-ray micro-tomography are composed of 256 (8 bits) or 65 536 (16 bits) grey levels, depending on the image reconstruction process. For comparison, both of these image types were used to calculate the density of the actual scanned specimens. In 8-bit images, the greyscale of X-ray micro-tomography images is coded between $n(x,y,z) = 0$ Hounsfield units (HU) for the darkest elements and $n(x,y,z) = 255$ HU for the brightest elements. Therefore, the highest value for n is 255 in 8-bit images, which corresponds to the value 65 535 in 16-bit images. The conversion from 16-bit to 8-bit images was directly done by the reconstruction algorithm. Since 8-bit images contain less grey levels, the greyscale histogram contains therefore less detail than that for 16-bit images.

Fig. 4 shows the greyscale histograms of images obtained from virgin and thermally oxidised 40% weight loss Gilsocarbon specimens. The greyscale histograms are composed of two distinct peaks. One of these peaks is located around the zero grey level and is due to the darkest, least attenuating, elements in the image, i.e. air environment and large pores within the material. The other peak is centred on a mean greyscale value ($\bar{n}$) and results from the image elements representing the graphite material. As it can be seen in Fig. 4, thermal oxidation decreases the mean grey level of the image and spreads out the histogram along the greyscale axis.

In this work, in order to describe the variation of density in the microstructure, both 8-bit and 16-bit images were used. Because the range of a 16-bit image greyscale is wider than 8-bit images, these types of image are more representative of the finer variation of density than 8-bit images. In 16-bit images, local densities were calculated using MATLAB subroutines, as described by Babout et al. [14]. The local density $\rho(x,y,z)$ (in kg m^{-3}) of an element was defined by

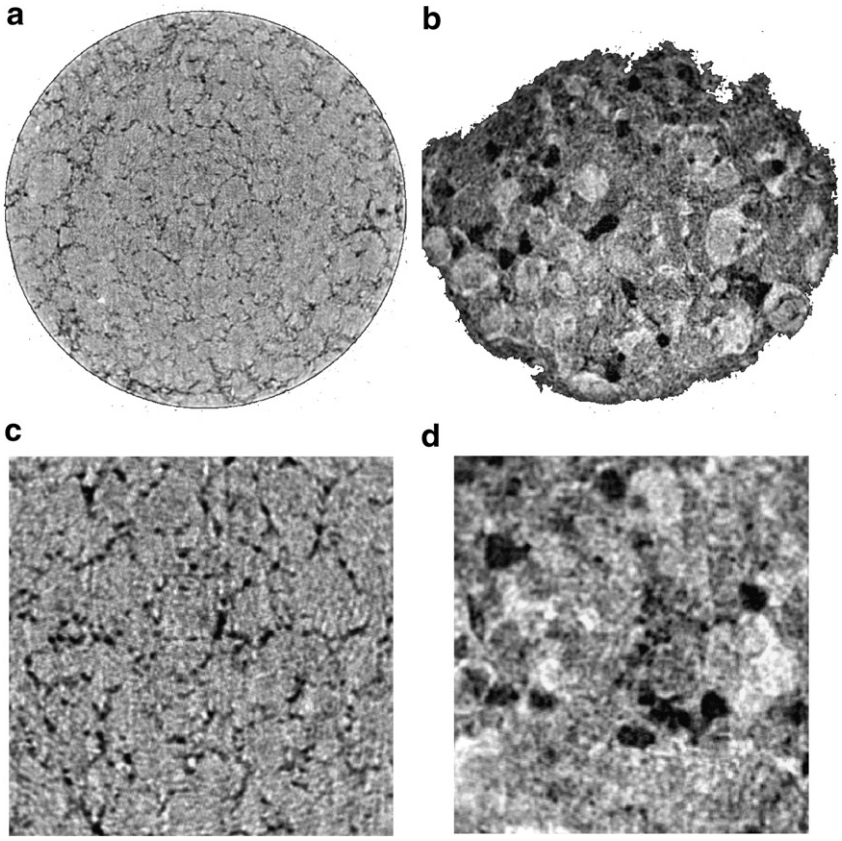

Fig. 3. Two-dimensional slices of the microstructure of (a and c) virgin and (b and d) of thermally oxidised Gilsocarbon; the main diameter of the specimens shown in (a) and (b) is about 9 mm; the areas shown in (c) and (d) are 3.8 mm × 3.8 mm.

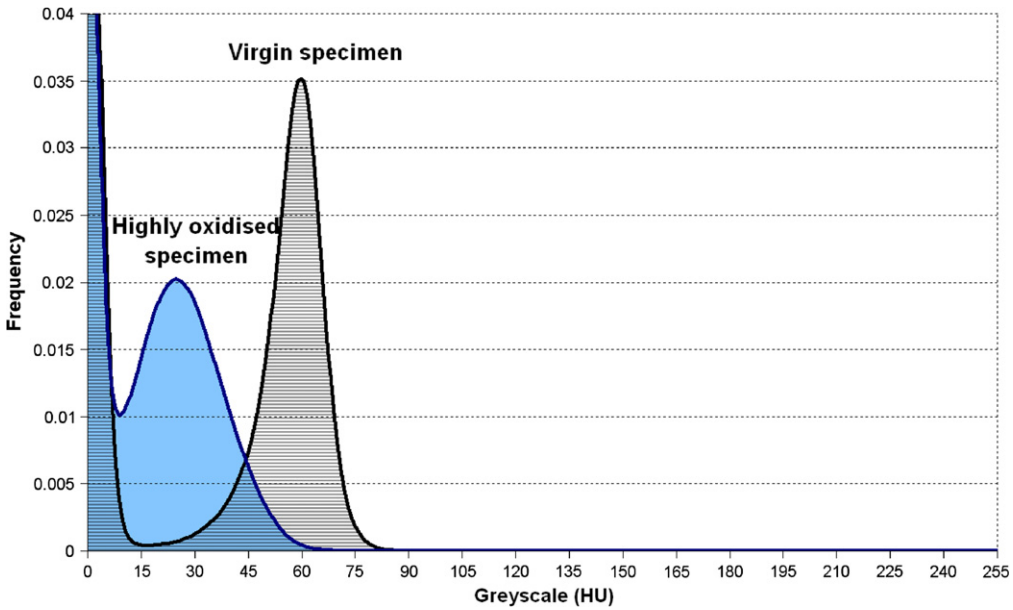

Fig. 4. Comparison between the greyscale histograms of tomographic images obtained from a virgin and a thermally oxidised 40% weight loss Gilsocarbon specimen. The greyscale uses 256 HU (Hounsfield units).

$$\rho(x,y,z) = \frac{n(x,y,z)}{\alpha}\left(\frac{\rho}{\mu}\right)_{\mathrm{HOPG}} \quad (2)$$

where $n(x,y,z)$ is the local 2^8 or 2^{16} level intensity (in Hounsfield units), μ is the attenuation factor (in m^{-1}) determined by the step-wedge method, and α is a scale factor arbitrarily set to $\alpha = 2.50\ cm^{-1}$ before reconstructing the image [14].

The bulk density of the samples was then calculated from the tomographic images by averaging local element densities in a volume containing 250 × 250 × 250 voxels extracted from a volume

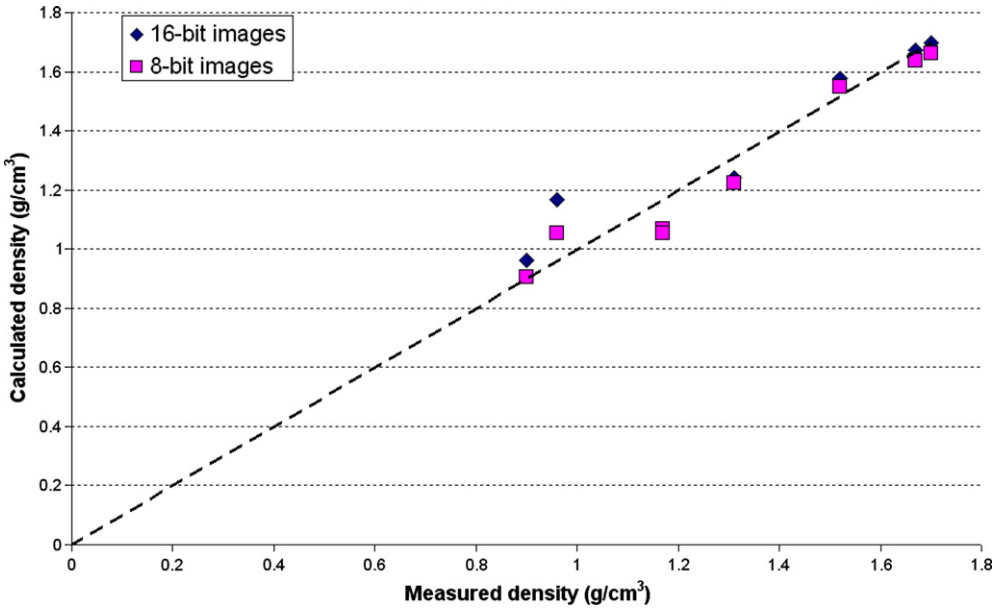

Fig. 5. Comparison between measured (dashed line) and calculated (diamond- and square-shaped plots) densities. The dashed line shows the 1:1 agreement between measurements and calculations.

in the centre of the dataset. Using 8-bit images, the average value of the image greyscale ($\bar{n}$) was calculated from the freely available software ImageJ [16]. The bulk density of the material ($\bar{\rho}$) was then directly calculated by averaging the expression of the local density given by Eq. (2) (in kg m^{-3}), thus leading to

$$\bar{\rho} = \frac{\bar{n}}{\alpha'}\left(\frac{\rho}{\mu}\right)_{\mathrm{HOPG}}, \tag{3}$$

where $\bar{n}$ is the average value of the image greyscale and α' is the corresponding scale factor for 8-bit images defined by $\alpha' = 2^8$, $\alpha = 256$, $\alpha = 640$ cm^{-1}.

With a voxel size of 19 μm, the volume of study was 100 mm^3. Densities were calculated from both 8-bit and 16-bit images using ImageJ[5] [16] and AMIRA[6] to select the region of the material and export the greyscale data into a text file. Because of the pre-processing, the analysis using 16-bit images required about an hour per image, but for 8-bit images, image pre-processing could be directly performed and the calculation process was most efficient in this case (a few minutes). In addition, densities calculated using Eq. (3) could be compared with those using the method described by Babout et al. [14]. The actual density of the specimens was known from weight and volume measurements before and after oxidation. The calculated densities were then compared to the actual density of the specimens (see [15]), (as shown in Fig. 5).

In Fig. 5, the dashed line represents the 1:1 agreement line between measurements of bulk density and calculations. The agreement between the image-based and measured densities of the samples is very good, although some minor discrepancies are present. Since the volume of calculation was extracted from the centre of the tomographic images of the bulk samples, a small degree of non-uniformity of thermal oxidation throughout the volume may be the cause of these minor discrepancies. The difference obtained using 8-bit and 16-bit images may be explained by the steep gradient of the greyscale histogram adjacent to the pores, i.e. between $n = 15$ HU and 20 HU for the highly oxidised specimen over a typical distance of three to five voxels (see Fig. 4). Since 8-bit images are coarser than 16-bit images, the difference between the calculated densities of oxidised specimens observed in Fig. 5 may be explained by the same thresholding effects resulting from image segmentation. Also, as it can be noticed from the comparison between the microstructures of virgin and thermally oxidised graphite made in Fig. 3, higher levels of oxidation seem to increase the mean size of the pores. Since the averaging volume is the same for virgin and thermally oxidised samples, the increase in the size of the pores, and therefore of the relative size of the pores in the model, may cause some of the discrepancies observed at higher oxidation levels.

2.4. Image segmentation

As previously described, image segmentation can be performed in applying an adequate greyscale threshold to obtain a suitable representation of the microstructure. The actual material is composed of a large range of pores having different sizes, some of which are sub-micron. Such very small pores are not thus directly visible using laboratory X-ray micro-tomography since the image resolution is in the micro-scale. However, these pores can significantly modify the attenuation and therefore the greyscale in the tomographic image. Fig. 6 shows a schematic representation of pores and their resulting binary partition after greyscale thresholding.

In tomographic images, actual pores (Fig. 6(a)) are represented by three-dimensional elements (voxels) whose greyscale varies according to the microstructural arrangement in the material (Fig. 6(b)). As it can be seen in Fig. 6(c), part of the microstructural information may be lost or transformed during image segmentation. This may also explain the difference observed in Fig. 5 between the mean densities of the oxidised specimens calculated using an 8-bit and a 16-bit image. The 8-bit image, coarser in greyscale levels than the 16-bit one, may affect the accuracy of the calculation. The density calculated using 8-bit images may thus appear lower than that calculated using 16-bit images. Fig. 7 shows a typical image segmentation result using the chosen greyscale threshold, i.e. $\bar{n} = 50$ HU on a two-dimensional slice from a tomographic image of virgin graphite. In Fig. 7, it can be seen that some features a few pixels in size are visible in the greyscale of the raw

[5] ImageJ website: http://rsb.info.nih.gov/ij/.
[6] AMIRA website: http://www.amiravis.com/ (Mercury Computer Systems).

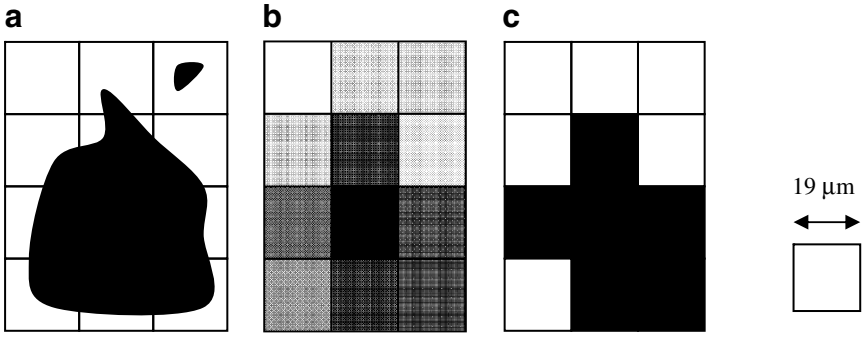

Fig. 6. Schematic representation (3×4 grid) of (a) an arbitrary two-dimensional area of the actual sample, (b) the same area after capture by X-ray micro-tomography and (c) image segmentation by greyscale thresholding.

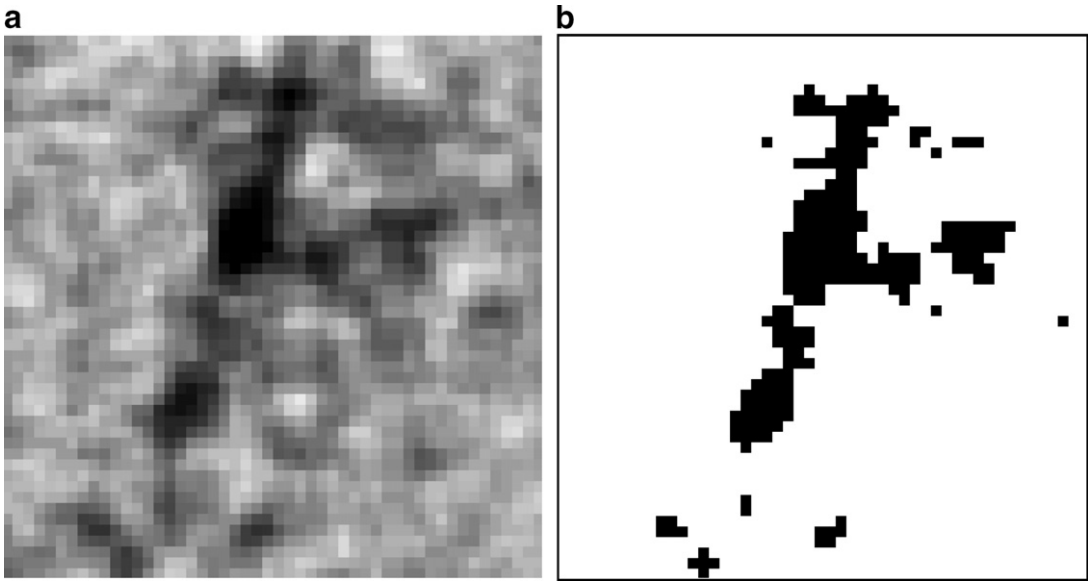

Fig. 7. Two-dimensional slice from the tomographic image of virgin Gilsocarbon (a) before and (b) after the application of a greyscale threshold $n(x,y,z) = 50$ HU; dimensions of the images are 0.95 mm × 0.95 mm (50 × 50 pixels).

image (Fig. 7(a)), but are removed by the application of a single greyscale threshold. Therefore, two-phase image segmentation of graphite images may lead to inaccurate or unrepresentative models. In this work, the use of a segmentation technique using the relationship between the element greyscale and the local density has been investigated, with the aim of obtaining more representative finite element models.

3. Multi-phase model

Based on microstructural models obtained from random Voronoi tessellations and tomographic images, Maire et al. [6] discussed the performance of finite element analysis algorithms. They found that dedicated finite element codes were more efficient at minimising the computer requirements than commercial codes because of their ability to reduce the amount of variables. In particular, the finite element software developed by Garboczi et al. [9,19] requires only 230 bytes per voxel. However, this software is limited to linear elastic analysis and has not been tested using multi-phase models. A commercial code was used in this work for greater flexibility, with a consequent cost in computational time.

In two-phase models, a clear distinction is made between fully solid material and porous phase. The solid phase is modelled as an ideal 'pore-free' material, while the porous phase has an elastic modulus of 0 GPa. In multi-phase models, a Young's modulus value is attributed to each 'intermediate' phase according to a local density/property relationship. The input Young's modulus in the models is thus also function of the brightness of the element in the X-ray micro-tomography dataset. In multi-phase models, one phase is defined by a group of elements having the same greyscale value. Since the greyscale value is related to the local density of the material scanned via Eq. (2), one phase of the model then includes all the elements corresponding to a same density. According to the greyscale of the original image, the definition of a multi-phase model requires the implementation of an input Young's modulus and of a failure criterion, both defined for each phase. In a previous paper [12], the present authors investigated the convergence of two-phase finite element models obtained from non-oxidised specimens. The results have shown that the solution was converging for resolutions below 40 μm. However, larger pores possibly increase the discrepancies between the models for thermally oxidised graphite.

3.1. Input Young's modulus

Using the Simpleware software [10], multi-phase models were generated from tomographic images of thermally oxidised speci-

mens of Gilsocarbon graphite. Each model contained approximately 70 phases of different density. The input Young's modulus of each phase, $E(\rho)$, was defined according to its calculated density, ρ, using the following relationship:

$$E(\rho) = A\rho^B. \quad (4)$$

This relationship Eq. (4) was fully defined using the Simpleware software and only requires to define the material parameters A and B. These two parameters were calculated using a fit to three data points for which the density and Young's modulus are known or can be determined. These three data points were selected at zero-density ($\rho = 0$ kg/m^3, $E = 0$ GPa), for virgin Gilsocarbon [1] ($\rho = 1810$ kg/m^3, $E = 10.85$ GPa) and at the theoretical 'pore-free' density of graphite, identical to the graphite crystal density, i.e. ($\rho_c = 2260$ kg/m^3, $E_0 = 19$ GPa). The value of the 'pore-free' Young's modulus (E_0) is not directly known from experiments, so its value was estimated from a two-phase finite element model of virgin graphite using a trial-and-error method. The input Young's modulus of the solid elements was adjusted until the calculated Young's modulus was equal to 10.85 GPa, which led to $E_0 = 19$ GPa. Replacing $E(\rho)$ and ρ in Eq. (4) by the above data, the following values for A and B were thus found:

$$A = 65\,363 \text{ GPa } (\text{kg/m}^3)^{-2.523} \text{and} \quad B = 2.523. \quad (5)$$

The determination of the parameters A and B are based on a few assumptions which could be further investigated in future works. Fig. 8 shows the relationship between the density and Young's modulus Eq. (4) obtained using the parameters A and B given by Eq. (5). Fig. 9 shows Young's modulus distribution in a multi-phase model for virgin Gilsocarbon graphite. Brighter, higher density elements have a higher Young's modulus and low density areas containing smaller pores are represented by darker elements. Multiple phases of different densities can hence be separated for which different mechanical properties can be defined according to the local density of the material. Elements having a Young's modulus close to zero have been removed from the models to avoid any numerical singularity during calculation by applying a greyscale threshold (n) equal to 3 HU, i.e. only elements denser than 90 kg/cm^3 were considered. The model was then divided into 70 phases equally distributed between densities of 90 kg/cm^3 and 2260 kg/cm^3. Hence, the input Young's modulus of each phase varied between 3.5 GPa and 19 GPa in the multi-phase models.

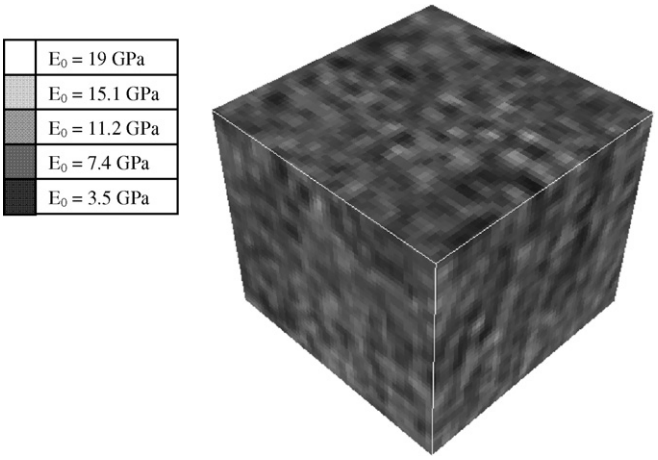

Fig. 9. Young's modulus distribution (E_0) in a multi-phase model for virgin graphite having a volume of $1 \times 1 \times 1$ mm^3 (~141 000 three-dimensional elements).

3.2. Strain-based failure model

Based on a smeared-crack approach, the ABAQUS CONCRETE option [11] was used to simulate the failure behaviour of graphite under tensile loading. This model was chosen to simulate the behaviour of Gilsocarbon before and after failure because of the similarities between the porous granular microstructures of concrete and Gilsocarbon. The finite element meshes generated from the tomographic images were composed of eight-noded cubic elements with reduced integration (ABAQUS C3D8R) to minimise the number of numerical singularities generated during calculation. The failure criteria implemented in the numerical models can be visualised by the schematic of the behaviour of each phase using the stress–strain curves as shown in Fig. 10 for four phases. In

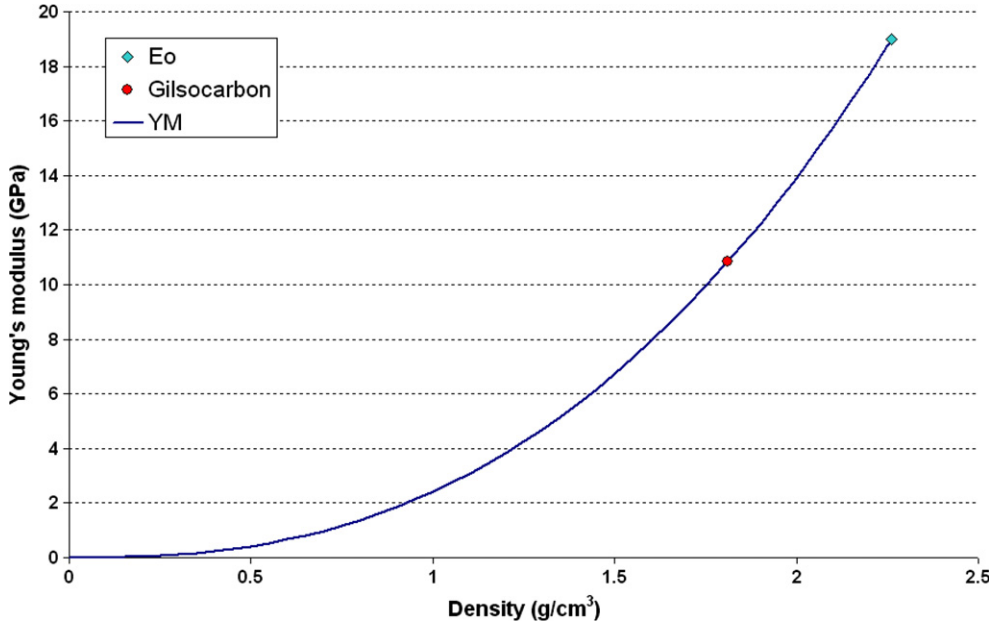

Fig. 8. Local relationship between Young's modulus (YM) and density; 'Eo' shows the estimated Young's modulus of a 'pore-free' graphite and 'Gilsocarbon' shows the experimental value for virgin Gilsocarbon [1].

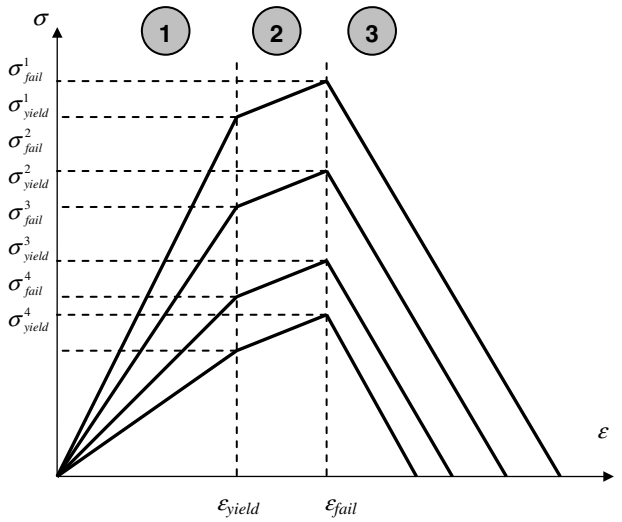

Fig. 10. Definition of a multi-phase strain-based failure model (four phases in this case).

Fig. 10, the first part of the stress–strain curves (denoted '1') is linear elastic and defined by Young's modulus of the phase. The concrete model requires the input of a yield strain ε_{yield}. In reality, yielding does not occur in graphite but the mechanical behaviour of virgin and oxidised graphite is not strictly linear [17], and an approximation to yield is therefore used during monotonic loading. Yoda et al. [18] studied the changes in dynamic Young's modulus of a quasi-isotropic graphite sample Grade IG-110 under axial tension. They found that the dynamic Young's modulus varied less than 1% for an applied strain up to 10^{-3}. Based on this result, the 'yield' strain in the model was assumed to be identical for each phase and equal to 10^{-3}, which corresponds to a 'yield' stress of 10.85 MPa from Young's modulus of virgin Gilsocarbon [1]. The slope of the stress–strain curve between the yield point and the start of failure (denoted '2' in Fig. 10) was defined according to the mechanical behaviour of virgin graphite between yield point and the start of failure, and was assumed to be identical for each phase. However, the value of the yield stress has been found not to greatly influence the calculation of the tensile strength from the model [13]. The corresponding maximum stress at failure of each phase was then calculated using the input Young's modulus of each phase and the slope of the stress–strain curve between the yield and failure strains. Using the quasi-brittle assumption for the graphite, the effective strain at failure of virgin graphite was calculated from its Young's modulus (E), i.e. 10.85 GPa, and tensile strength (σ_{fail}), i.e. 17.5 MPa [1], as

$$\varepsilon_{fail} = \sigma_{fail}/E = 1.6 \times 10^{-3}. \quad (6)$$

The strain at failure (ε_{fail}) was assumed to be the same for all phases, which allows for different critical stresses (σ_{fail}) according to the phase definition. Denser parts of the model will therefore fail at a higher critical stress than parts of lower density. After the initiation of failure, the stress in the failed element was assumed to decrease linearly towards zero (part denoted '3' in Fig. 10). The slope of the stress–strain curve after failure of an element, the so-called tension stiffening, was calibrated from the numerical model of virgin Gilsocarbon graphite in order to avoid a premature end to the analysis due to numerical singularities generated after the point of failure.

Under compression, the input stress–strain curve was similar to that employed under tension. However to account for the ratio of the compressive strength (σ_c = 70 MPa) to the tensile strength (σ_t = 17.5 MPa) of virgin Gilsocarbon [1], the magnitude of the input compressive stress at which failure occurs was set to fourfold that in tension (σ_c/σ_t). Poisson's ratio was taken as equal to 0.21 [1] for both tension and compression, and assumed to be independent of the local density.

4. Numerical results and comparison with experimental data

The input mechanical properties thus defined, i.e. Young's modulus and non-elastic behaviour, were then implemented into multi-phase models derived from the actual microstructure of non-oxidised and thermally oxidised specimens. It was assumed that the local relationships between greyscale, density and input properties were independent of the degree of oxidation of the bulk specimen. This assumption was based on the fact that thermal oxidation locally decreases the density, and therefore the grey level of the corresponding elements in the tomographic image, which then results in the decrease of the local input mechanical properties in the finite element model.

Numerical models were then subjected to a numerically applied tension with an applied tensile strain equal to $\bar{\varepsilon} = 0.01$. The effective Young's modulus was calculated from multi-phase models by a linear elastic analysis and the failure model was implemented in the calculation to numerically determine the tensile and compressive strengths. The effective tensile and compressive strengths were both calculated from the average maximum load at the surface of the model perpendicular to the applied displacement.

4.1. Changes in Young's modulus with thermal oxidation

A linear analysis was conducted using finite element models containing about 100 000 cubic elements. These models required about 10 GBytes of memory and less than 1 h on a supercomputer using 8 processors running at 1.6 GHz each. In this study, with 19-μm resolution images, the volume of each model was limited to 1 mm^3. Changes in Young's modulus with thermal oxidation were calculated for models having a pore volume fraction (P) between 27% and 66%. Fig. 11 shows the numerical results obtained using both the new multi-phase and the earlier two-phase finite element models [13]. Experimental data for thermally oxidised quasi-isotropic nuclear grades IM1-24 [20] and IG-110 [21] are also shown in Fig. 11 as a comparison. Although IM1-24 is coarse grained and IG-110 is fine grained, these two grades have comparable physical properties. The density of IM1-24 grade, i.e. 1850 kg/m^3, is close to that of IG-110, i.e. 1750 kg/m^3 and both grades are quasi-isotropic. Young's modulus of IM1-24, i.e. 12.4 GPa [22], is relatively close to that of IG-110 which is 9.61 GPa in the longitudinal direction and 10.2 GPa in the transverse direction [23].

Fig. 11 shows quite close agreement between the predicted changes in effective Young's modulus using the two-phase and multi-phase models. These two numerical models obtain the decreasing trend of Young's modulus with oxidation observed in the experiments. In the two-phase models, it is clear that calculated pore volume fractions under-estimate the actual porosity in the specimens since some models derived from the tomography data contained only 10% of porosity. However, because smaller, unobserved, pores are also taken into account in the multi-phase models, these models seem to be more representative of the actual microstructure of the material than two-phase models.

Experimental results for the effects of thermal oxidation reported by Imai et al. [21] show a smooth decreasing trend, and are in good agreement with those obtained by Pickup et al. [20]. As described in the Appendix, Young's modulus is related to the pore fraction contained in the material or model by Knudsen's semi-empirical equation [24,25]:

$$E = E_0 \exp(-b_P P), \quad (7)$$

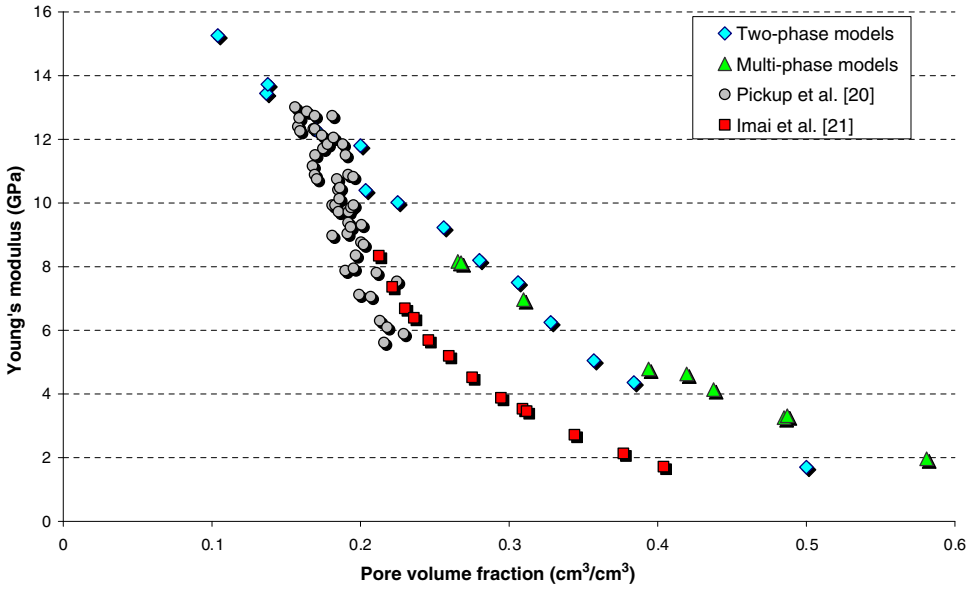

Fig. 11. Young's modulus changes with increasing pore volume fractions calculated using two-phase models [8], multi-phase models and comparison with experimental data obtained from IM1-24 grade [20] and IG-110 grade [21].

where E_0 is the virtually 'pore-free' Young's modulus and b_P is the decay factor (see Appendix).

In Knudsen's relationship Eq. (7), the two dominant characters of the pores are described by their amount (P) and their aspect ratio (b_P), as shown by Buch [26]. For comparison, experimental and numerical results are reported using Knudsen's relationship in Table 1 where ΔP is the difference between the pore volume fraction before (P_i) and after (P_f) oxidation (see Appendix). Table 1 shows that the decrease in Young's modulus, measured by the decay factor (b_P) in Knudsen's equation, occurs faster in the experiments than predicted by the numerical models. Since the b_P is related to the shape of the pores, this result then suggests that both finite element models are too stiff due to missing porosity or inaccurate shape ratio. The slower decrease of the calculated Young's modulus might be explained by the development of very fine narrow nano-pores during thermal oxidation [20]. These elongated pores could be due to the greater reactivity of the carbon atoms at the edge of the basal plane than those in the middle. Although they might represent a very small portion of the overall amount of porosity, the elongated shape of these pores could have a significant effect on the overall behaviour of the material because of the high stress concentrations generated at the tip of these pores [3]. These stress concentrations would then contribute to the decrease of Young's modulus in thermal oxidised specimens. Because X-ray micro-tomography operates at the micro-scale, these very small pores would then not be accurately represented in the numerical models, which could explain the discrepancy observed between experimental values and numerical predictions.

Table 1
Comparison between numerical and experimental changes in Young's modulus with thermal oxidation using Knudsen's equation Eq. (7)

Source	ΔP (P_i–P_f) (cm^3/cm^3)	Decay factor (b_P)	E_0 (GPa)
Two-phase models	0.11–0.5	4.1	19
Multi-phase models	0.27–0.58	4.8	30
[20]	0.18–0.23	7.0	40.7
[21]	0.225–0.41	7.9	42

4.2. Stress analysis in non-elastic models

In the non-elastic models, a uniform displacement was numerically applied to one face of the finite element models until failure occurred. Due to the very large number of elements and to memory limitations, the volume of the model was reduced to $40 \times 40 \times 40$ cubic elements (ABAQUS C3D8R), i.e. 0.75 mm^3 using a 19-μm resolution image. For non-linear analysis, the maximum number of elements allowed in a model was about 64 000, which required ~14 GB of memory. Eight parallel processors cadenced at 1.6 GHz were used for the calculation. The finite element models were subjected to tension, and the same structures were also subjected to compression. In both cases calculations were run until final failure occurs. The strain at failure varied between 1.4×10^{-3} for the oxidised models and 2.5×10^{-3} for the virgin ones. In models for virgin graphite, tensile and compressive stresses were found to be evenly distributed throughout the volume, but higher stress areas were present in models for oxidised graphite. As expected, in models for oxidised graphite, pore closure occurs by elastic deformation during compression and allows stresses to propagate through the material.

Fig. 12 shows some stress–strain curves obtained during numerically applied tension until final cracking was obtained. These are for the multi-phase models containing pore volume fractions between 0.27 cm^3/cm^3 and 0.66 cm^3/cm^3. The tensile strength predicted by the models, i.e. maximum stress, decreases with increasing pore volume fraction. The turn-around obtained just before cracking is due to tension stiffening effects after failure initiation in the numerical models. This tension stiffening was necessary to limit the number of numerical singularities generated during the analysis [13], and is an artefact of the model. Although there are some variations, e.g. $P = 0.59$ cm^3/cm^3, the strain at failure (i.e. at the peak load) is generally reduced by thermal oxidation. This result is different than that obtained from microstructural models which simulated radiolytically oxidised graphite [8], in which it was found that the strain at failure increased with increasing artificial pore volume fraction. The decreasing strain at failure with increasing thermal oxidation might then be explained by the influence of the pore distribution

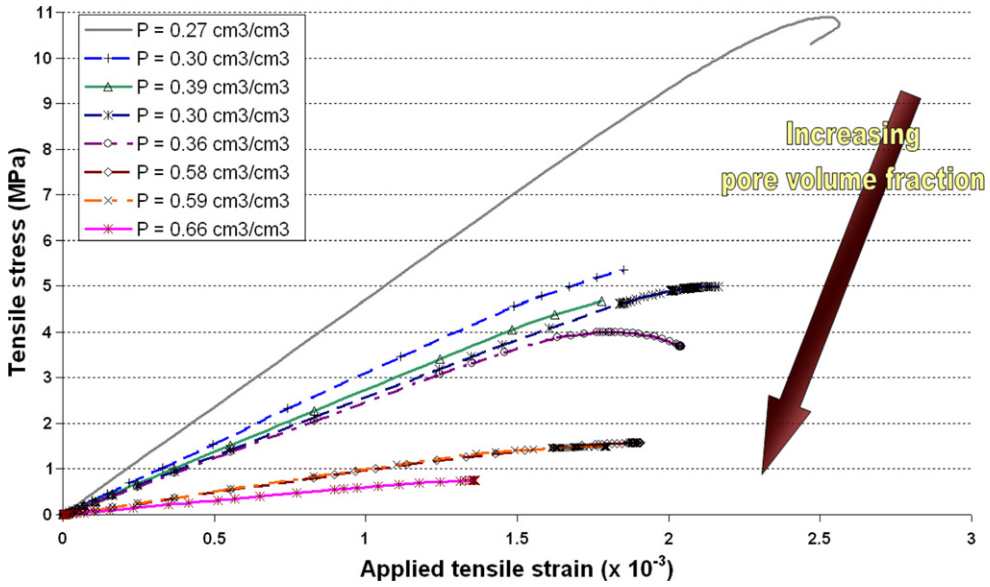

Fig. 12. Calculated stress–strain curves in multi-phase models for thermally oxidised Gilsocarbon graphite under numerically applied tension.

in the models and by the larger size of the pores in thermally oxidised specimens than in models simulating radiolytic oxidation. This is due to the higher stress concentrations resulting from the narrow and elongated shape of the pores in the thermally oxidised specimens. However, the relative small size of the models, compared to the large size of the pores, may also cause this difference. In the case of simulated radiolytically oxidised models, the maximum pore size was approximately equal to that contained in virgin graphite, i.e. about 0.5 mm in diameter. However, thermal oxidation increases this value to about 1 mm in diameter in the models taken from the image, which can be more in the actual thermally oxidised material. Therefore, the maximum pore size is relatively large compared to the size of thermally oxidised models. This may have an effect on the predicted strength.

4.3. Changes in tensile strength with thermal oxidation

In the stress–strain curves obtained from the models, the tensile strength is defined by the maximum stress reached by the model subjected to a uniform, numerically applied tension. The changes in tensile strength were calculated from the multi-phase models of thermally oxidised Gilsocarbon for the full range of porosity. With the two-phase models, only pore volume fractions below $P = 0.50\ \mathrm{cm}^3/\mathrm{cm}^3$ could be considered due to the substantial loss of load path in models containing higher pore volumes. With multi-phase models, this problem did not occur and higher levels of pore volume fraction could be considered.

The bend strength of 30 Gilsocarbon specimens, thermally oxidised using the same oxidation procedure as described in [15], was measured using three-point bending experiments. The specimens were rectangular, 6 mm × 6 mm × 18 mm, and had a 45° V-notch of 1 mm depth at mid-span. An INSTRON 1195 instrumentation device was used for the three-point bend tests; no post-oxidation treatment was used before mechanical testing; the central displacement of the cross-head was set to 0.5 mm per min. The bend strength (σ_B) of these specimens was thus determined. Using these measurements, the tensile strength of the specimens (σ_t) was calculated assuming that the ratio between tensile and bend strength remain constant with oxidation, i.e. $\sigma_t/\sigma_B = 0.69$, as calculated for virgin Gilsocarbon [1]. In Fig. 13, numerical results obtained using two-phase models and multi-phase models are plotted against the pore volume fraction. These numerical results are compared to experimental data for the tensile strength of Gilsocarbon specimens thermally oxidised at different levels. Fig. 13 shows a very good agreement between the numerical predictions obtained from the multi-phase models and the experimental data, and is better than the agreement obtained with the two-phase model. The tensile strength after oxidation can be expressed using Knudsen's relationship written as [24,27,28]:

$$\sigma_t = \sigma_0 \exp(-b_P P), \tag{8}$$

where σ_0 is the tensile strength of a virtually 'pore-free' graphite and b_P is the decay factor (see Appendix).

Numerical and experimental changes in tensile strengths can be compared for a pore volume fraction range (ΔP) using Eq. (8), as shown in Table 2. It was found that numerical results obtained from a multi-phase model are slightly above those obtained by a two-phase model, with a decay factor (b_P) around 6. In the experimental data, the decay coefficient is 8.7. The reasons for this difference could be similar to the calculations of Young's modulus, since the development of stress in the microstructure is related to the elastic modulus.

4.4. Changes in compressive strength with thermal oxidation

An experimental study of the changes in compressive strengths of thermally oxidised Gilsocarbon specimens was conducted at the University of Hull. The environmental conditions during thermal oxidation and the experimental testing procedure were identical to those described in [15]. The experimental data thus obtained were used for comparison with the numerical results obtained using the multi-phase models. The two-phase finite element models could not be used for compression due to the complexity involved in modelling contact between the surfaces of the empty pores. This problem does not arise in the multi-phase models because of the better numerical stability of these models. Fig. 14 compares the numerical and experimental compressive strengths for increasing pore volume. As shown in Fig. 14, numerical compressive strengths obtained using multi-phase models were found to be in very good agreement with experimental data. The general trend of experimental and numerical compressive strength with increasing thermal oxidation is very similar in both cases. In Fig.

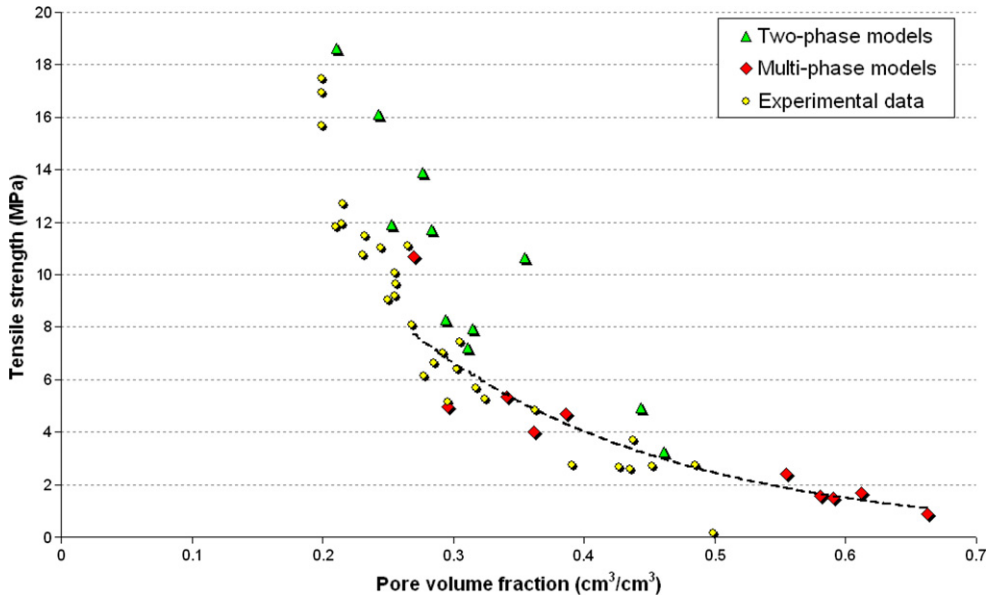

Fig. 13. Comparison between tensile strength changes with increasing pore volume fractions obtained from two-phase models, multi-phase models and experimental data. The dashed line shows the general trend of tensile strength calculated by multi-phase models.

Table 2
Comparison between numerical and experimental tensile strengths obtained from bend strength measurements

Source	ΔP (P_i–P_f) (cm^3/cm^3)	Decay factor (b_P)	σ_0 (MPa)
Two-phase models	0.19–0.48	5.77	57
Multi-phase models	0.27–0.66	6.03	89
Experimental tensile strength (from three-point bending measurements)	0.2–0.5	8.7	88

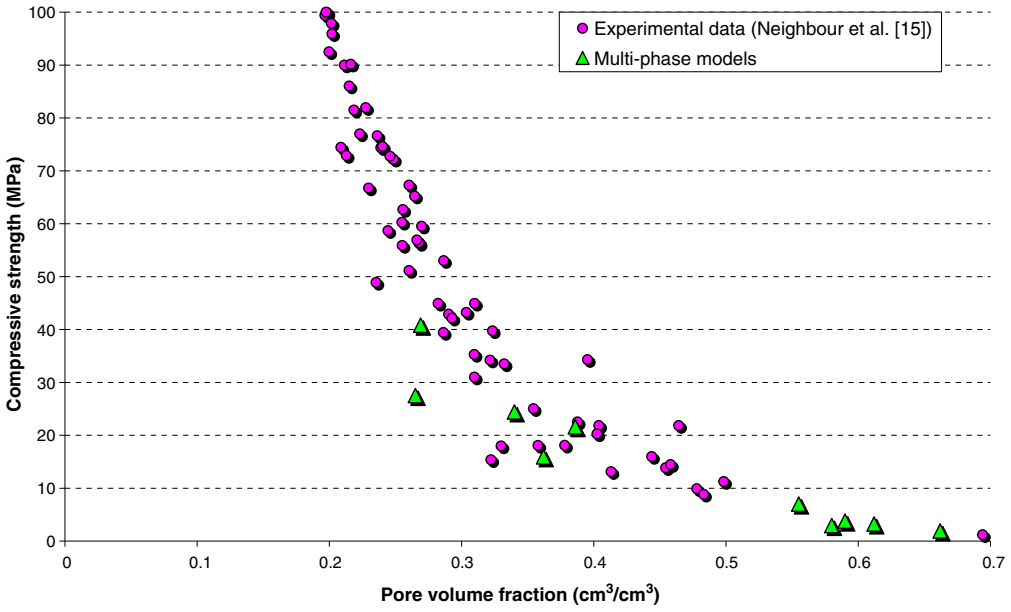

Fig. 14. Comparison between compressive strength changes with increasing pore volume fraction obtained from the multi-phase models and experimental testing [15].

14, it can also be noted that the virgin Gilsocarbon samples tested in this study had a higher compressive strength than those tested by Kelly and Brocklehurst [1]. Using Knudsen's relationship [24,27,28], the compressive strength is expressed in terms of pore volume fraction (P) by

$$\sigma_c = \sigma_c^0 \exp(-b_P P), \tag{9}$$

where σ_c^0 is the compressive strength of a virtually 'pore-free' graphite and b_P is the decay factor.

In Table 3, Knudsen's relationship was used to compare the changes in compressive strength with increasing pore volume fraction resulting from thermal oxidation. Eqs. (A8) and (A9), derived in the Appendix, were used to express Knudsen's equation in terms of pore volume fractions for comparison.

Table 3
Comparison between changes in compressive strength obtained from the multi-phase models and from compression tests using Knudsen's relationship

Source	ΔP (P_i–P_f) (cm^3/cm^3)	Decay factor (b_P)	σ_c^0 (MPa)
Multi-phase models	0.27–0.66	7.65	615
Experimental compressive strengths	0.2–0.7	7.97	457

As shown in Table 3, the numerical predictions obtained using the models are in good agreement with the experimental measurements. In the experimental and numerical results, it was generally found that compressive strengths were less scattered than tensile strengths. In the numerical models subjected to tension, the tensile strength calculated largely depends on the biggest pore whereas the model seems more stable in compression. This result suggests that, possibly due to the closure of the pores during compression, compressive tests would be less sensitive to the microstructural heterogeneity than tensile tests.

5. Discussion

Overall, it was generally observed that multi-phase models should provide a better representation of the actual specimen than two-phase models since they do not rely on a single greyscale threshold. However, although multi-phase models can take the influence of smaller pores into account, two-phase and multi-phase models were found to provide very similar predictions for changes in Young's modulus with increasing pore volume fraction. The modulus predictions for both numerical the multi- and two-phase models were slightly greater than the experimental data. A possible explanation for this result was the formation of very fine slit-shaped nano-pores during thermal oxidation, which might not be entirely captured in the finite element models.

The calculated tensile strengths obtained using a strain-based failure model and based on graphite local microstructural stress–strain and tensile strength characteristics were compared with experimental data obtained from thermally oxidised Gilsocarbon. It was found that the strain at failure generally decreased with increasing thermal oxidation. This result may be explained by the larger pores induced by thermal oxidation and possibly an effect of the relatively small size of the numerical models compared to the size of the pores. These large pores may influence the stress propagation within the models in applied tension, ultimately leading to critical cracking earlier.

The predicted tensile strengths provided good agreement with experimental data and with numerical calculations obtained using the two-phase models. With two-phase models, only porosities less than 50% could be considered due to the substantial loss of load path in models with higher pore volumes [8]. With the multi-phase models, this problem did not occur and therefore higher levels of pore volume fraction can be considered. Single phase models could not be used for compressive loadings however, because of their improved numerical stability, the multi-phase models allowed compression modelling. The numerical predictions for compressive strength gave very good agreement compared with the experimental data. The main advantage of a multi-phase model over a two-phase model is shown to be its capacity of modelling compressive strength and high weight losses due to better numerical stability.

Although it was found that the spatial resolution of the models showed little influence on the elastic results for non-oxidised graphite, the development of larger pores in more oxidised specimens may reduce the accuracy of the method, especially when applied with a non-elastic model. The size of the averaging box may also influence the convergence of the numerical solution because of the relative size of the pore contained in the volume. The future development of computational power should allow for larger volumes, and indeed eventually graphite components, to be studied. This work can be extended to other properties such as thermal conductivity, electrical conductivity and coefficient of thermal expansion and other failure models could also be applied. It is felt that further work would be required to develop more efficient three-dimensional failure models and finite element tools for the elastic and non-elastic analysis of very large microstructural models.

6. Conclusions

- Comparison with experimental data of the prediction of modulus and strength of thermally oxidised nuclear graphite, using a density based, multi-phase microstructural model is presented.
- The segmentation into multiple phases of an X-ray microtomography image, based on density, allowed the resulting finite element model not to rely on a single arbitrarily set greyscale threshold to segment the microstructure, as is the case with previous two-phase modelling.
- Numerical predictions of the tensile strength changes with increasing pore volume fractions due to thermal oxidation compared well with experimental data and with other numerical results obtained using two-phase models.
- Multi-phase models are more representative of the graphite microstructure than two-phase models although numerical predictions of strength and modulus were similar in both cases. However, multi-phase models could be used to represent higher weight loss and could be used to model compressive loading, whereas the two-phase model could not. This is because the multi-phase models are numerically more stable than two-phase models.
- Compressive strengths calculated from multi-phase models were in good agreement with experimental values.
- Compressive tests were also found to be less sensitive to the microstructure geometry than was the case for tensile tests. This is possibly because pore closure occurs in compression.

Acknowledgements

British Energy Generation Ltd. is gratefully acknowledged for their financial support (Contract No. GRA/GNSR/6023). The views expressed in this paper are those of the authors and do not necessarily represent those of the sponsor.

Appendix

Mechanical property changes with oxidation can be expressed in terms of fractional weight loss or pore volume fraction contained by the material. The following appendix reviews the mathematical expressions of the relationship between Young's modulus changes with oxidation. The degree of thermal oxidation is measured by the corrected weight loss coefficient (x), which is a measure of the bulk density of the material before oxidation (ρ_0) and after oxidation (ρ), and can be written as

$$x = \frac{\rho_0 - \rho}{\rho_0}. \tag{A1}$$

The pore volume fraction (P) of the material is related to the bulk density (ρ) by

$$P = \frac{\rho_c - \rho}{\rho_c}, \tag{A2}$$

where $\rho_c = 2.26\ \mathrm{g/cm^3}$ is the theoretical density of graphite crystal.

The pore volume fraction (P) is related to the fractional weight loss (x) by

$$P = 1 - \frac{\rho_0}{\rho_c}(1 - x). \tag{A3}$$

Using Eqs. (A1) and (A3), the pore volume fraction changes (ΔP) of a material after oxidation are related to the fractional weight loss (x) by

$$\Delta P = P_f - P_i = (1 - P_i)x. \tag{A4}$$

Thus, the pore volume fraction (P) is also a measure of the degree of oxidation. This Eq. (A4) is similar to that obtained by Burchell et al. [3].

Knudsen's relationship, which is essentially an exponential decay function, is often used to express a given mechanical property in terms of fractional weight loss after oxidation (x) or in terms of pore volume fraction (P). Changes due to thermal oxidation are related on the microstructure by increasing pore volume fractions (P). The Young's modulus is related to the pore volume fraction (P) by [24,25]:

$$E = E_{(P=0)} \exp(-b_P P), \tag{A5}$$

where b_P is a parameter representing the rate of Young's modulus changes with increasing pore volume fractions, and $E_{(P=0)}$ is the initial Young's modulus which can be obtained by extrapolating the curve fitting the data to zero pore volume fraction ($P = 0$). Although it can be shown that b_P depends on the pore shape ratio [26], it is generally determined by experiments.

Similarly, Young's modulus after oxidation (E) can be expressed in terms of fractional weight loss (x) by

$$E = E_{x=0} \exp(-b_x x), \tag{A6}$$

where $E_{x=0}$ is Young's modulus before oxidation and b_x is the decay factor.

In Eq. (A6), using the expression of the pore volume fraction (P) given by Eq. (A5), the following expression is obtained for the final Young's modulus after oxidation:

$$\begin{aligned} E_f &= E_{(P_i)} \exp\left(-b_x \frac{P_f - P_i}{1 - P_i}\right), \\ &= E_{(P_i)} \exp\left(-\frac{b_x}{1 - P_i} P_f\right) \exp\left(\frac{b_x P_i}{1 - P_i}\right). \end{aligned} \tag{A7}$$

Identifying the terms in Eq. (A7) with those in Eq. (A6), we obtain an expression for the virtually 'pore-free' Young's modulus and for the decay factor b_P in terms of b_x:

$$E_{(P=0)} = E_{(P_i)} \exp\left(\frac{b_x P_i}{1 - P_i}\right), \tag{A8}$$

$$b_P = \frac{b_x}{1 - P_i}. \tag{A9}$$

Experimental data for oxidised materials are often presented in terms of weight loss (x). Eqs. (A8) and (A9) are therefore very useful to express Knudsen's relationship in terms of pore volume fractions and facilitate the comparison with data expressed either in terms of fractional weight loss or pore volume fractions. Similar equations can also be obtained for other properties following Knudsen's relationship such as strength, thermal conductivity, electrical resistivity, etc.

References

[1] J.E. Brocklehurst, B.T. Kelly, Carbon 31 (1993) 155.
[2] R.E. Nightingale, Nuclear Graphite, Academic Press, London, 1962.
[3] T.D. Burchell, I.M. Pickup, B. McEnaney, R.G. Cooke, Carbon 24 (1986) 545.
[4] F. Lasagni, A. Lasagni, E. Marks, C. Holzapfel, F. Mücklich, H.P. Degischer, Acta Mater. 55 (2007) 3875.
[5] L. Babout, P.M. Mummery, T.J. Marrow, A. Tzelepi, P.J. Withers, Carbon 43 (2005) 765.
[6] E. Maire, A. Fazekas, L. Salvo, R. Dendievel, S. Youssef, P. Cloetens, J.M. Letang, Compos. Sci. Technol. 63 (2003) 2431.
[7] E. Maire, P. Colombo, J. Adrien, L. Babout, L. Biasetto, J. Eur. Ceram. Soc. 27 (2007) 1973.
[8] C. Berre, S.L. Fok, B.J. Marsden, L. Babout, A. Hodgkins, T.J. Marrow, P.M. Mummery, J. Nucl. Mater. 352 (2006) 1.
[9] E.J. Garboczi, A.R. Day, J. Mech. Phys. Solids 43 (1995) 1349.
[10] Simpleware, ScanFE and ScanIP Reference guide Version 2.0, 2004.
[11] HKS, Hibbit, Karlsson and Sorensen Inc., ABAQUS/Standard version 6.5 manual, 2006.
[12] C. Berre, S.L. Fok, B.J. Marsden, G.B. Neighbour, Finite element modelling of the effects of porosity changes on the mechanical properties of nuclear graphite, International Carbon Conference, Aberdeen, United Kingdom, 16–21st July 2006.
[13] C. Berre, S.L. Fok, B.J. Marsden, P.M. Mummery, J. Ali, T.J. Marrow, G.B. Neighbour, Failure analysis of the effects of porosity in thermally oxidised nuclear graphite using finite element modelling, in: Proceedings of 7th International Nuclear Graphite Spec. Meeting, Oak Ridge National Lab., USA, 10–13th September 2006.
[14] L. Babout, T.J. Marrow, P.M. Mummery, P.J. Withers, Scripta Mater. 54 (2006) 829.
[15] G.B. Neighbour, P.J. Hacker, Mater. Lett. 51 (2001) 307.
[16] M.D. Abramoff, P.J. Magelhaes, S.J. Ram, Biophoton. Int. 11 (2004) 36.
[17] G.M. Jenkins, Brit. J. Appl. Phys. 13 (1962) 30.
[18] S. Yoda, M. Eto, T. Oku, J. Nucl. Mater. 119 (1983) 278.
[19] C.H. Arns, M.A. Knackstedt, W.V. Pinczweski, E.J. Garboczi, Geophysics 67 (2002) 1396.
[20] I.M. Pickup, B. McEnaney, R.G. Cooke, Carbon 24 (1986) 535.
[21] H. Imai, K. Fujii, T. Kurosawa, S. Nomura, J. Nucl. Mater. 118 (1983) 294.
[22] P. Ouagne, G.B. Neighbour, B. McEnaney, J. Phys. D. Appl. Phys. 38 (2005) 1259.
[23] T. Eto, M. Oku, Nucl. Eng. Design 143 (1993) 239.
[24] F.P. Knudsen, J. Am. Ceram. Soc. 42 (1959) 376.
[25] R.M. Spriggs, J. Am. Ceram. Soc. 44 (1961) 628.
[26] J.D. Buch, A Theoretical Deviation of the Knudsen Relationship 16th Carbon Conference, San Diego, USA, 1983.
[27] E. Ryshkewitch, J. Am. Ceram. Soc. 36 (1953) 65.
[28] W. Duckworth, J. Am. Ceram. Soc. 36 (1953) 68.